Synthesis of Metamaterial Enhancing Lenses for Improving the Radiation Performance of Existing Linear Antenna Arrays

M. Salucci, G. Oliveri, N. Anselmi, G. Gottardi, and A. Massa

Abstract

This work presents an innovative material-by-design (*MbD*) technique for the improvement of the radiation features (in terms of beam-width, directivity and side-lobe level) of existing linear scanned arrays. The developed strategy exploits a suitably customized quasi conformal transformation optics (*QCTO*) technique to synthesize meta-material radomes with reduced anisotropy as well as a source inversion (*SI*) strategy in order to let the original array mimic the radiation performance of significantly larger apertures. Some numerical results are presented ad discussed in order to validate the effectiveness of the *MbD* approach and its suitability to improve the radiation characteristics of linear arrays.

1 Extensive Analysis - Half-Cosine Profile - $h' = 4.0$ [λ], $l' = 0.0$ [λ], $t' = 9.0$ [λ], $N = 15$

1.1 Step 1: Expanding the physical array ($N = 15$, $L = 7.0$ [λ])

Input Parameters

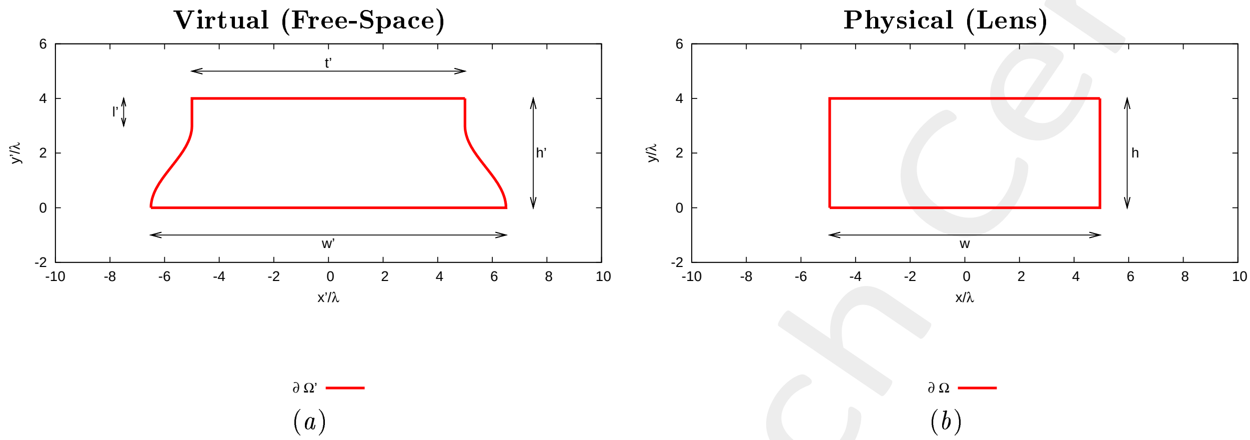

Figure 1: Transformation regions. The lower side of both virtual and physical boundaries are supposed to be PEC.

- **Virtual Geometry**

# Test Case	h' [λ]	l' [λ]	t' [λ]	w' [λ]
1	4.0	0.0	9.0	**10.3**
2	4.0	0.0	9.0	**11.3**
3	4.0	0.0	9.0	**12.1**
4	4.0	0.0	9.0	**12.9**
5	4.0	0.0	9.0	**13.6**

Table I: Considered virtual geometries. The values of w' have been empirically determined in order to achieve an aperture of the virtual array (L') equal to a multiple of $\lambda/2$. It is imposed that $h = h'$, while w is not controlled by the user.

- **Physical Array**
  - Number of elements, spacing, aperture: $N = 15$, $d = \frac{\lambda}{2}$, $L = 7.0$ [λ];
  - Positions: $x_n \in [-L/2, L/2]$, $y_n = \frac{\lambda}{4}$, $n = 1, ..., N$;
  - Steering angle: $\phi_s = 90.0$ [deg];
  - Excitations: $I_n = 1.0$, $\varphi_n = \frac{-2\pi}{\lambda} x_n sin\left(\phi_s + 90\right)$; $n = 1, ..., N$;
- **QCTO**
  - Discretization cell dimension: 0.05 [λ] (0.01 [λ] for source mapping);

1.1.1 Results

Resulting aperture of the virtual array (L') - for step 2

- The aperture of the virtual array (L') is computed after mapping the physical array into the virtual space;
- The resulting number of equi-spaced elements is computed as

$$N' = round\left(\frac{L'}{0.5} + 1\right)$$

	Virtual Geometry				**Virtual Array**	
# Test Case	h' [λ]	l' [λ]	t' [λ]	w' [λ]	L' [λ]	N'
1	4.0	0.0	9.0	**10.3**	7.52	**16**
2	4.0	0.0	9.0	**11.3**	8.02	**17**
3	4.0	0.0	9.0	**12.1**	8.49	**18**
4	4.0	0.0	9.0	**12.9**	9.01	**19**
5	4.0	0.0	9.0	**13.6**	9.52	**20**

Table II: Resulting aperture and number of equi-spaced elements of the virtual array after expanding the physical array.

1.2 Step 2: Compressing the virtual array ($N' > N$, $L' > L$ [λ])

Input Parameters

- **Virtual Array**
  - Number of elements, spacing, aperture: $N' = \{16; 17; 18; 19; 20\}$, $d' = \frac{\lambda}{2}$, $L' = \{7.5; 8.0; 8.5; 9.0; 9.5\}$ [λ];
  - Positions: $x'_n \in [-L'/2, L'/2]$, $y'_n = \lambda/4$, $n = 1, ..., N'$;
  - Steering angle: $\phi_s = 90.0$ [deg];
  - Excitations: $I'_n = 1.0$, $\varphi'_n = \frac{-2\pi}{\lambda} x_n sin\,(\phi_s + 90)$; $n = 1, ..., N'$;
- **Virtual Geometry:** same of step 1;
- **QCTO:** same of step 1.

1.3 Source Inversion (SI)

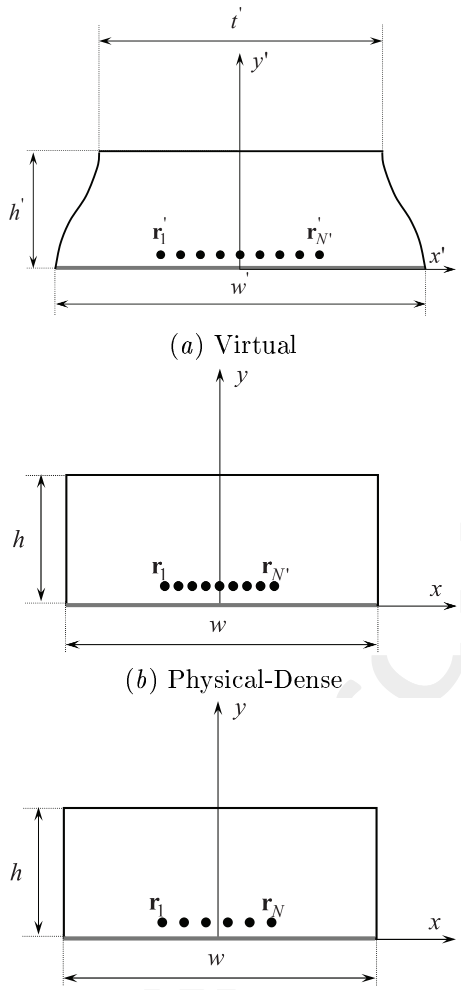

(c) Physical-SI

Figure 2: Geometry for (a) the virtual array in free-space, (b) the "physical-dense" array inside the lens and (c) the physical-SI array inside the lens.

Parameters

- Before SI
  - Number of elements: $N' = \{16; 17; 18; 19; 20\}$, $d' < \lambda/2$;
- After SI
  - Number of elements after SI: $N = 15$, $d = \frac{\lambda}{2}$;
  - Aperture: $L = 7.0$;
- Radius of the observation domain: $r_{SI} = 50.0$ [λ];
- Number of field sampling points: $n_{SI} = 1000$.

1.3.1 Near-Field Distribution ($\phi_s = 90$ [deg], $f = 600$ [MHz])

Case $w' = 10.3$ **[**λ**]**, $N' = 16$

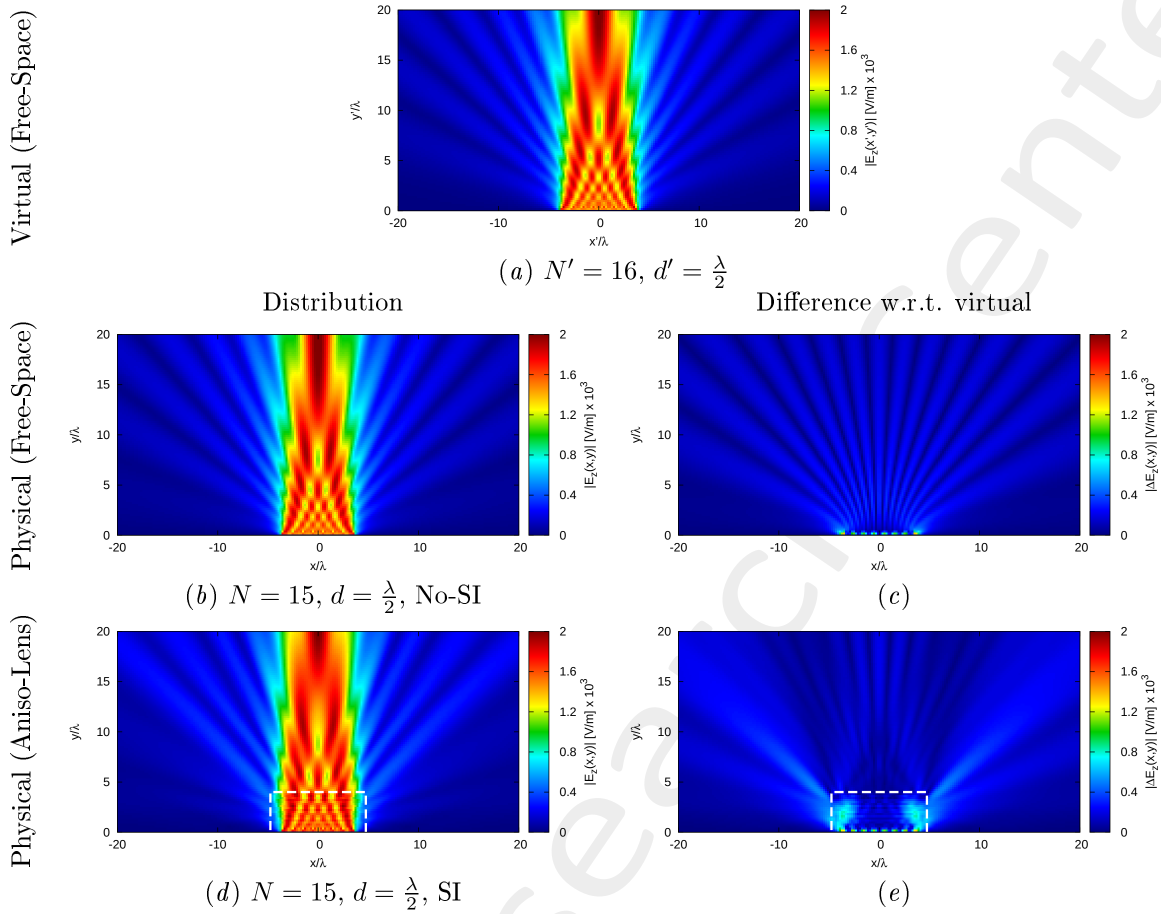

Figure 3: $\phi_s = 90$ [deg], $f = 600$ [MHz] - Electric field distributions.

Case $w' = 11.3$ **[**λ**],** $N' = 17$

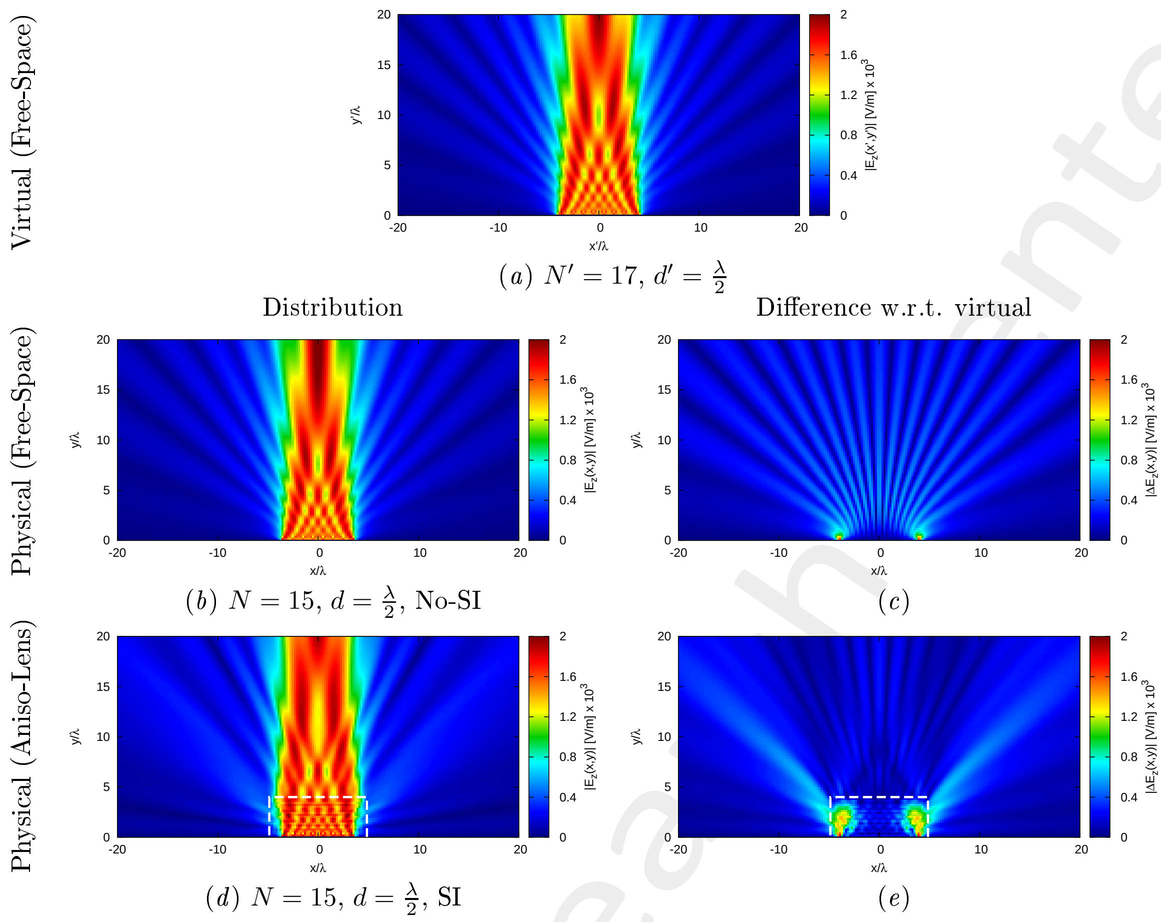

Figure 4: $\phi_s = 90$ [deg], $f = 600$ [MHz] - Electric field distributions.

Case $w' = 12.1$ **[**λ**],** $N' = 18$

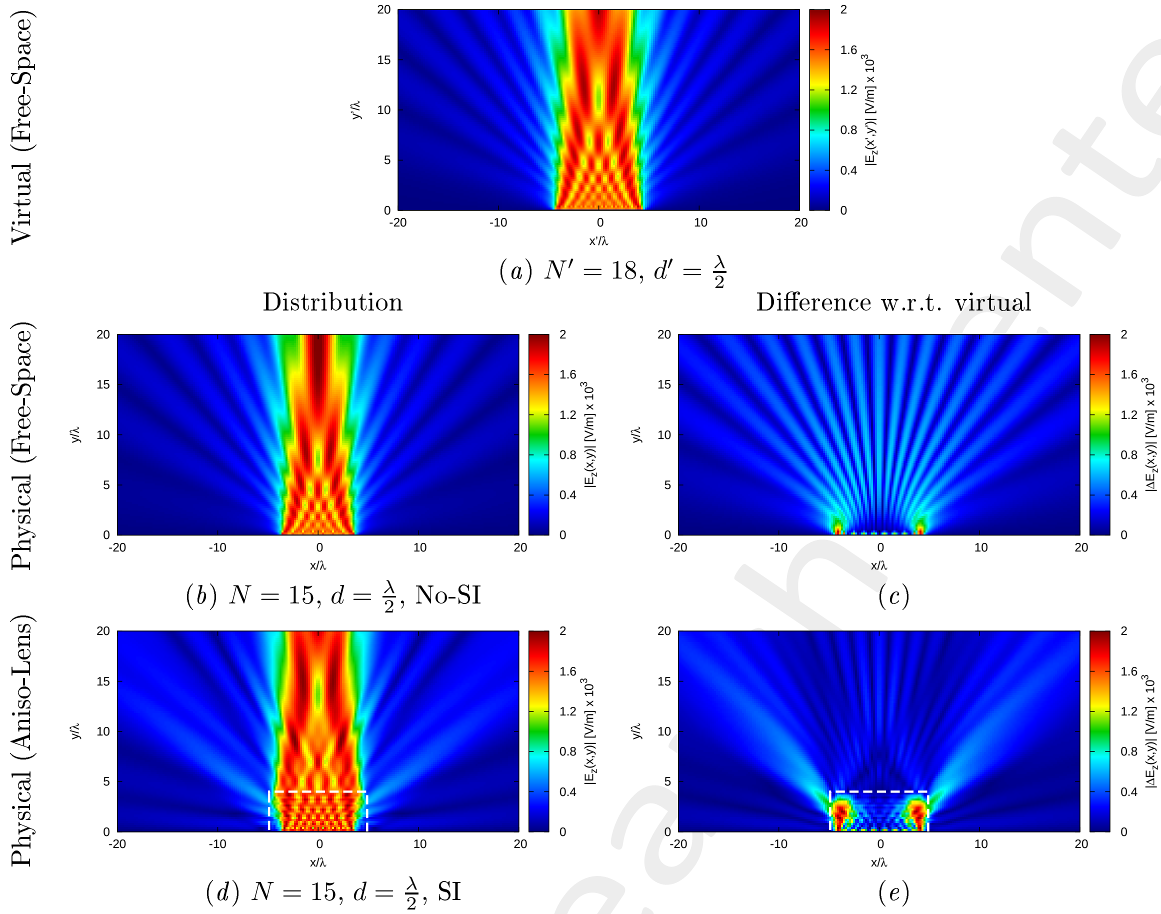

Figure 5: $\phi_s = 90$ [deg], $f = 600$ [MHz] - Electric field distributions.

Case $w' = 12.9$ **[**λ**],** $N' = 19$

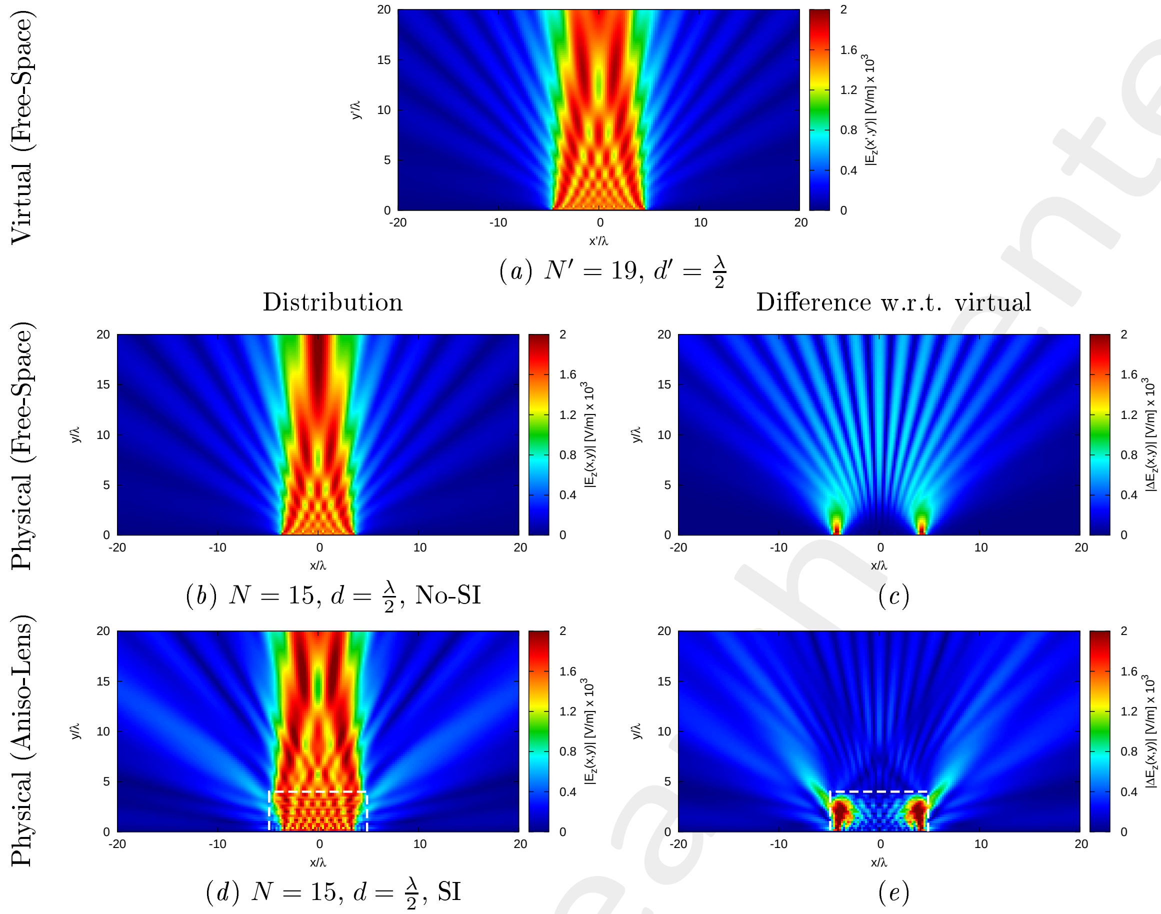

Figure 6: $\phi_s = 90$ [deg], $f = 600$ [MHz] - Electric field distributions.

Case $w' = 13.6$ **[λ],** $N' = 20$

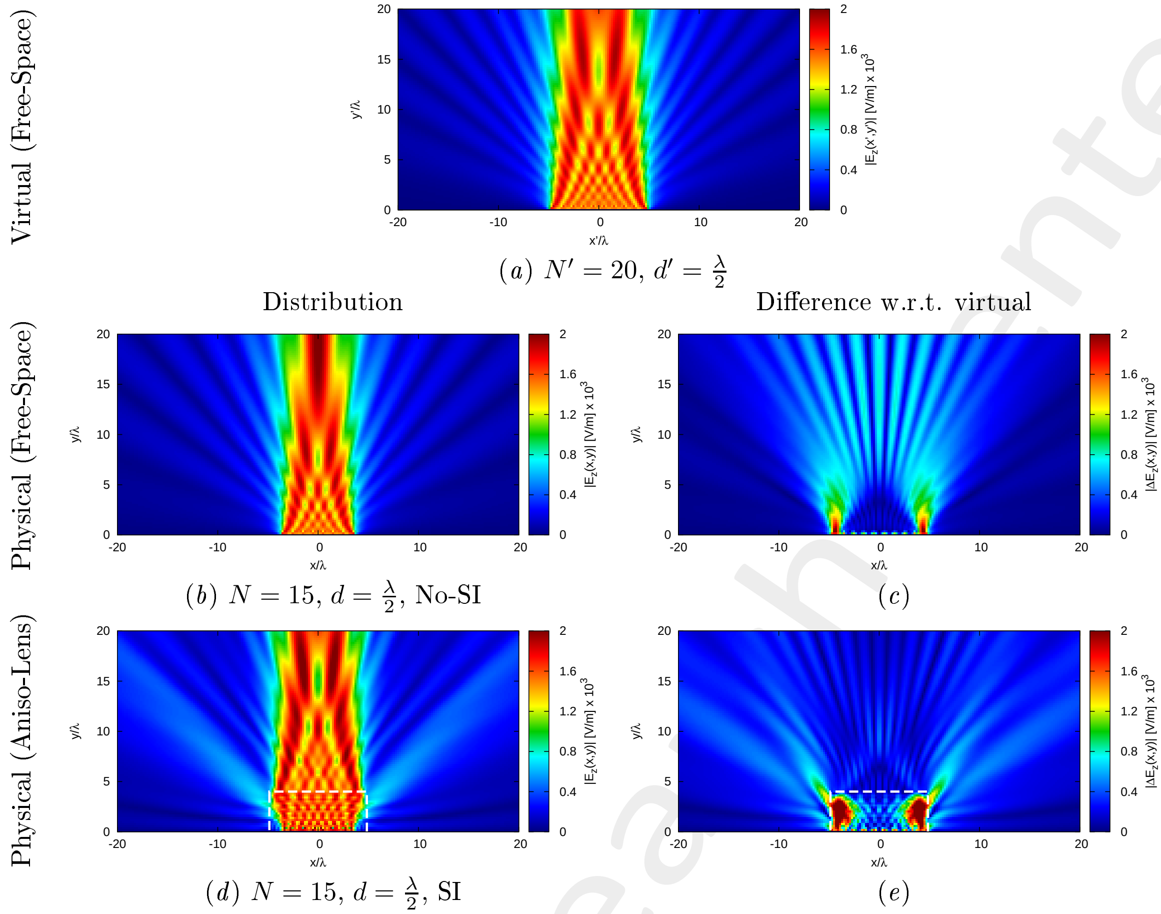

(a) $N' = 20$, $d' = \frac{\lambda}{2}$

(b) $N = 15$, $d = \frac{\lambda}{2}$, No-SI

(c)

(d) $N = 15$, $d = \frac{\lambda}{2}$, SI

(e)

Figure 7: $\phi_s = 90$ [deg], $f = 600$ [MHz] - Electric field distributions.

1.3.2 Near-Field Distribution ($\phi_s = 75$ [deg], $f = 600$ [MHz])

Case $w' = 10.3$ **[**λ**]**, $N' = 16$

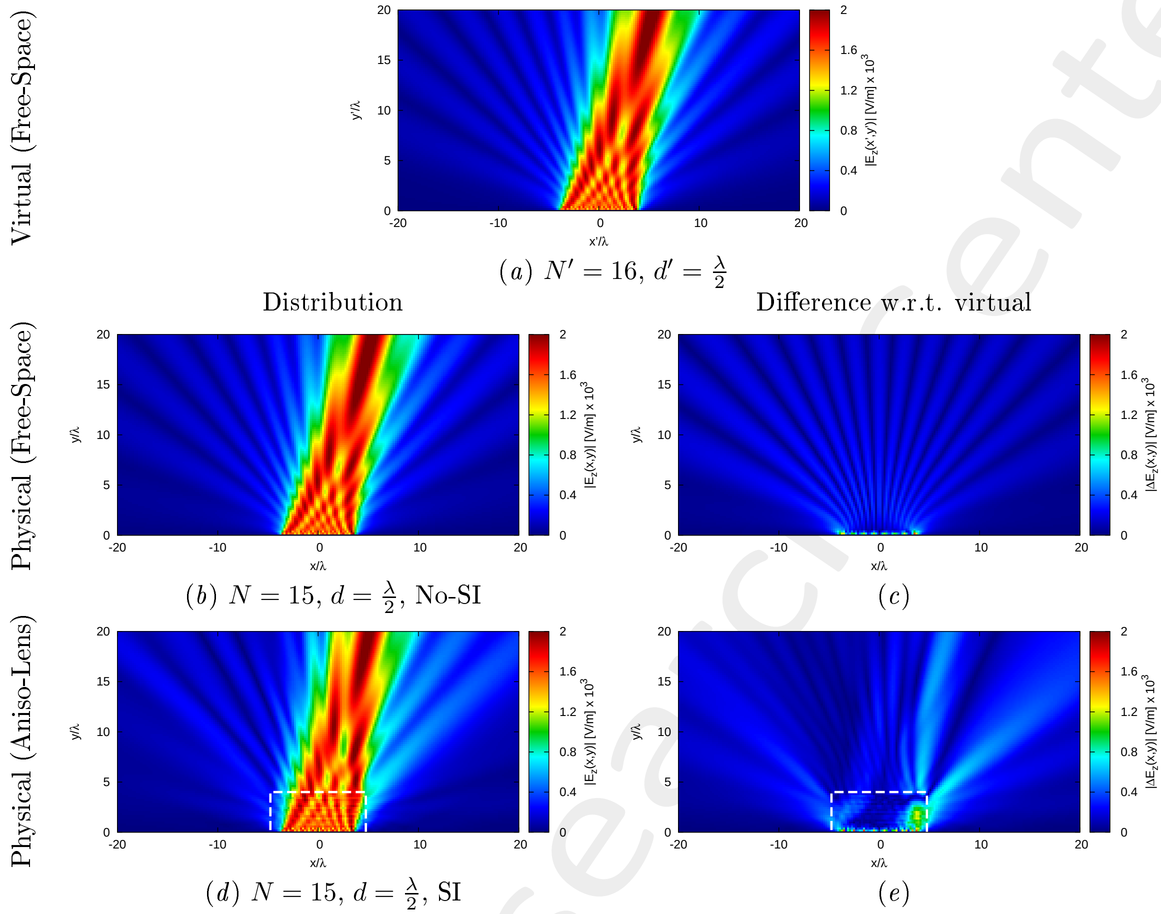

Figure 8: $\phi_s = 90$ [deg], $f = 600$ [MHz] - Electric field distributions.

Case $w' = 11.3$ **[**λ**]**, $N' = 17$

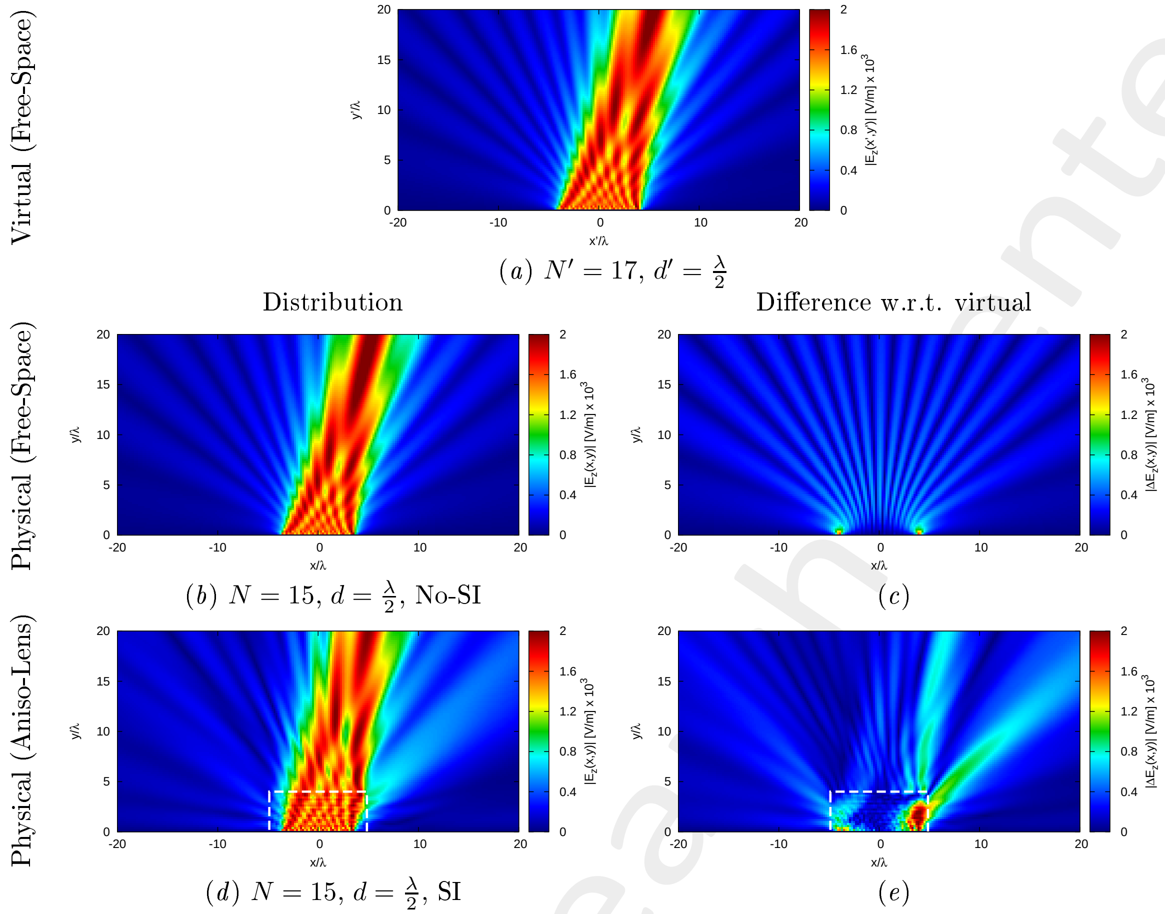

Figure 9: $\phi_s = 90$ [deg], $f = 600$ [MHz] - Electric field distributions.

Case $w' = 12.1$ **[**λ**]**, $N' = 18$

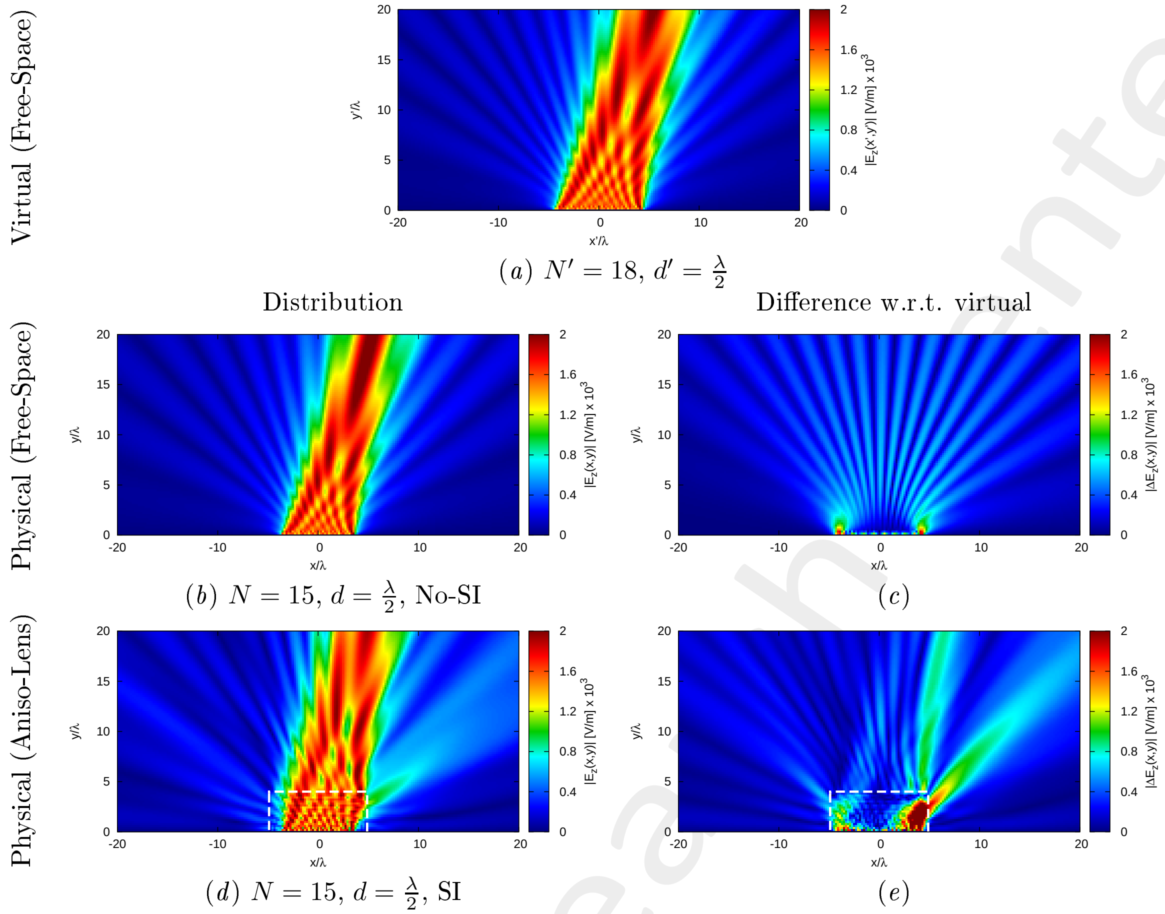

Figure 10: $\phi_s = 90$ [deg], $f = 600$ [MHz] - Electric field distributions.

Case $w' = 12.9$ **[**λ**],** $N' = 19$

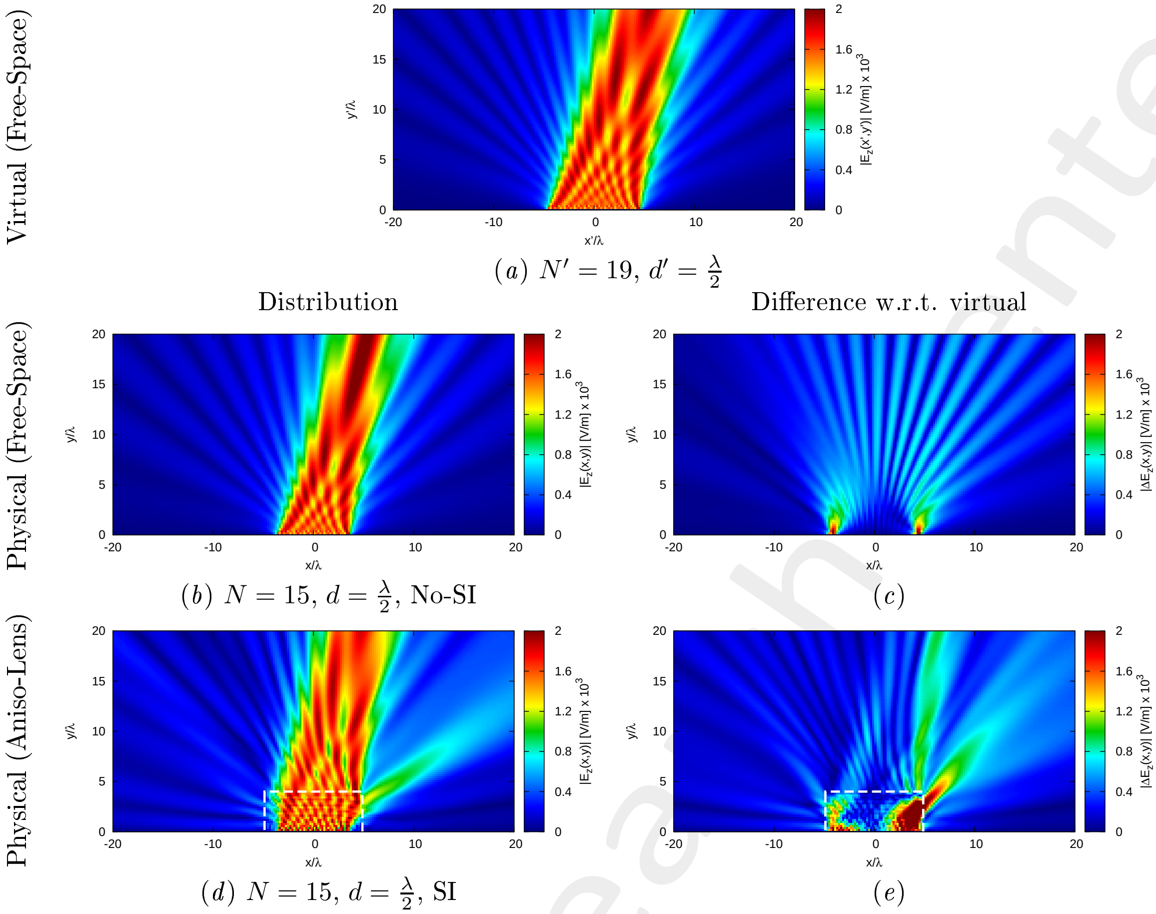

Figure 11: $\phi_s = 90$ [deg], $f = 600$ [MHz] - Electric field distributions.

Case $w' = 13.6$ **[**λ**]**, $N' = 20$

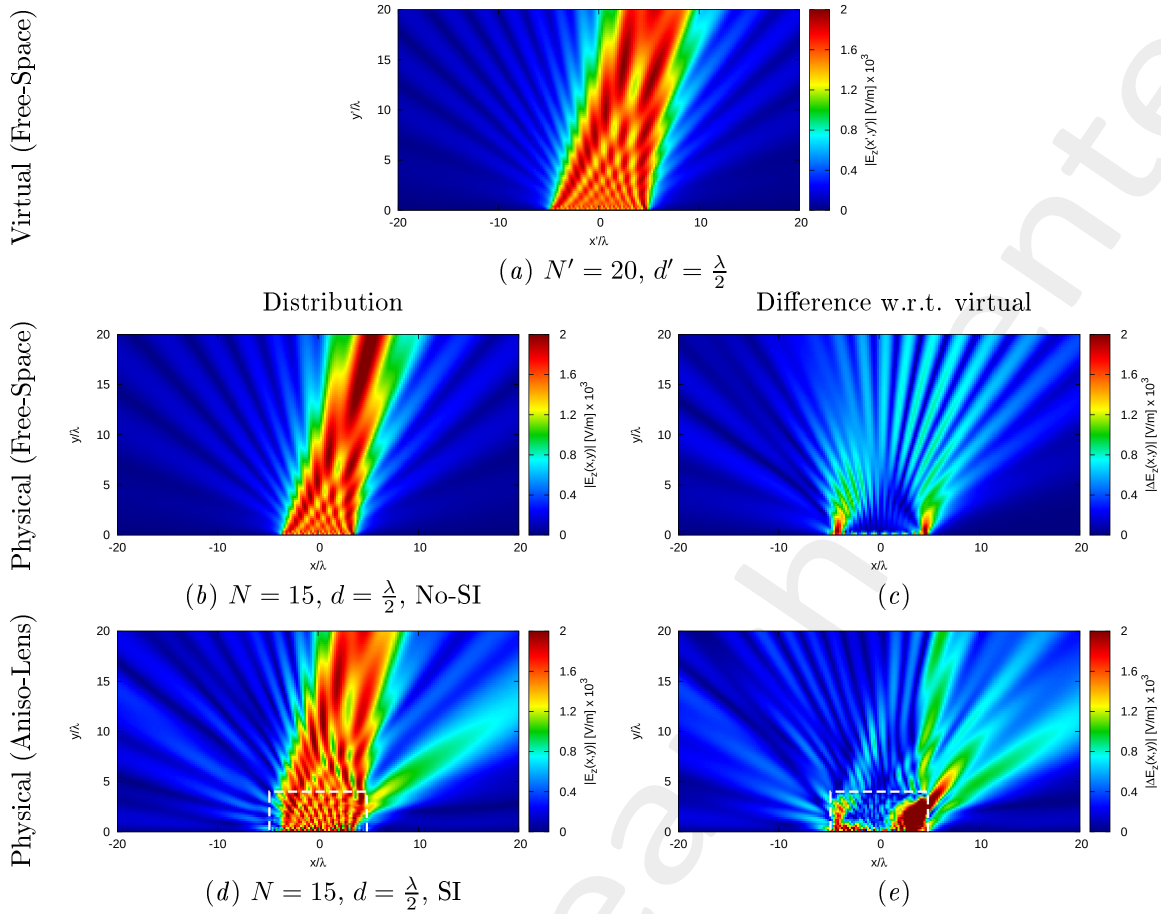

(a) $N' = 20$, $d' = \frac{\lambda}{2}$

(b) $N = 15$, $d = \frac{\lambda}{2}$, No-SI

(c)

(d) $N = 15$, $d = \frac{\lambda}{2}$, SI

(e)

Figure 12: $\phi_s = 90$ [deg], $f = 600$ [MHz] - Electric field distributions.

1.3.3 Near-Field Distribution ($\phi_s = 60$ [deg], $f = 600$ [MHz])

Case $w' = 10.3$ [λ], $N' = 16$

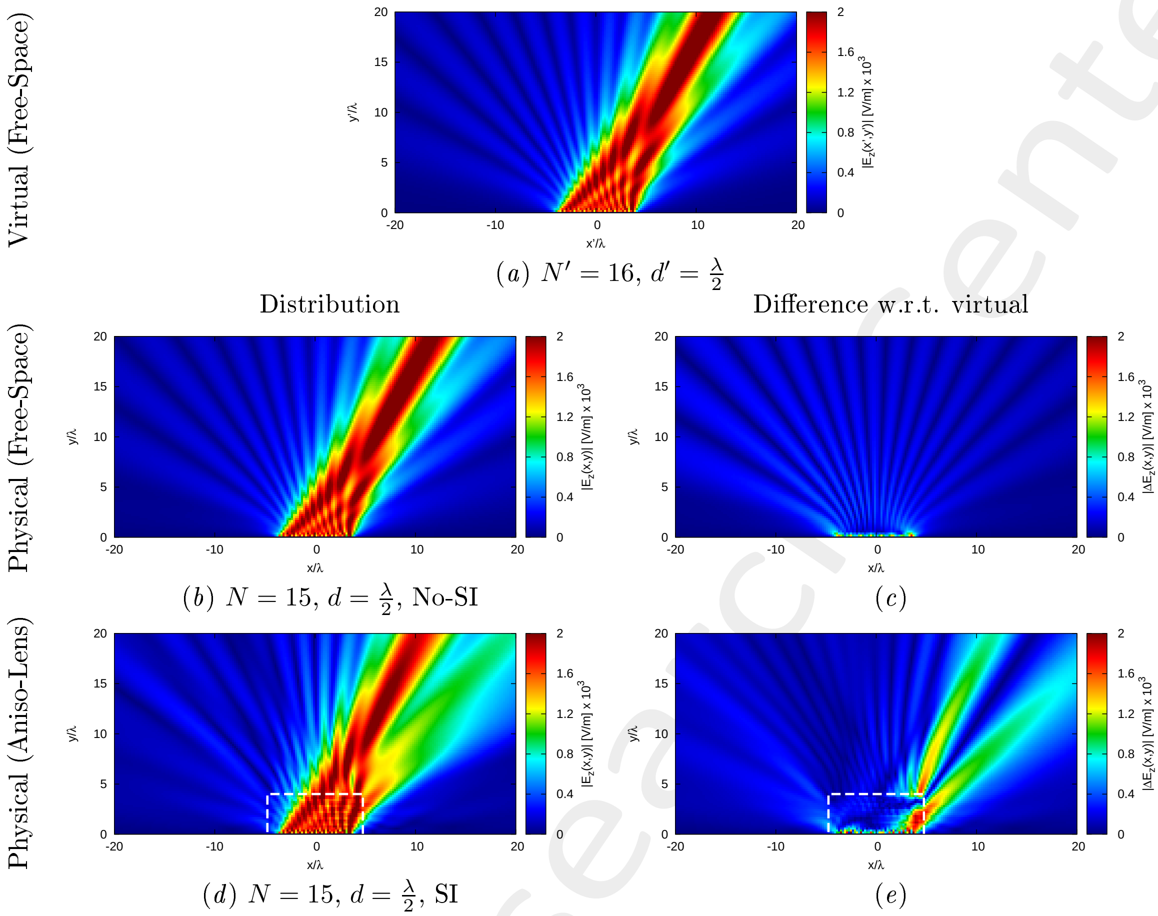

Figure 13: $\phi_s = 90$ [deg], $f = 600$ [MHz] - Electric field distributions.

Case $w' = 11.3$ **[**λ**],** $N' = 17$

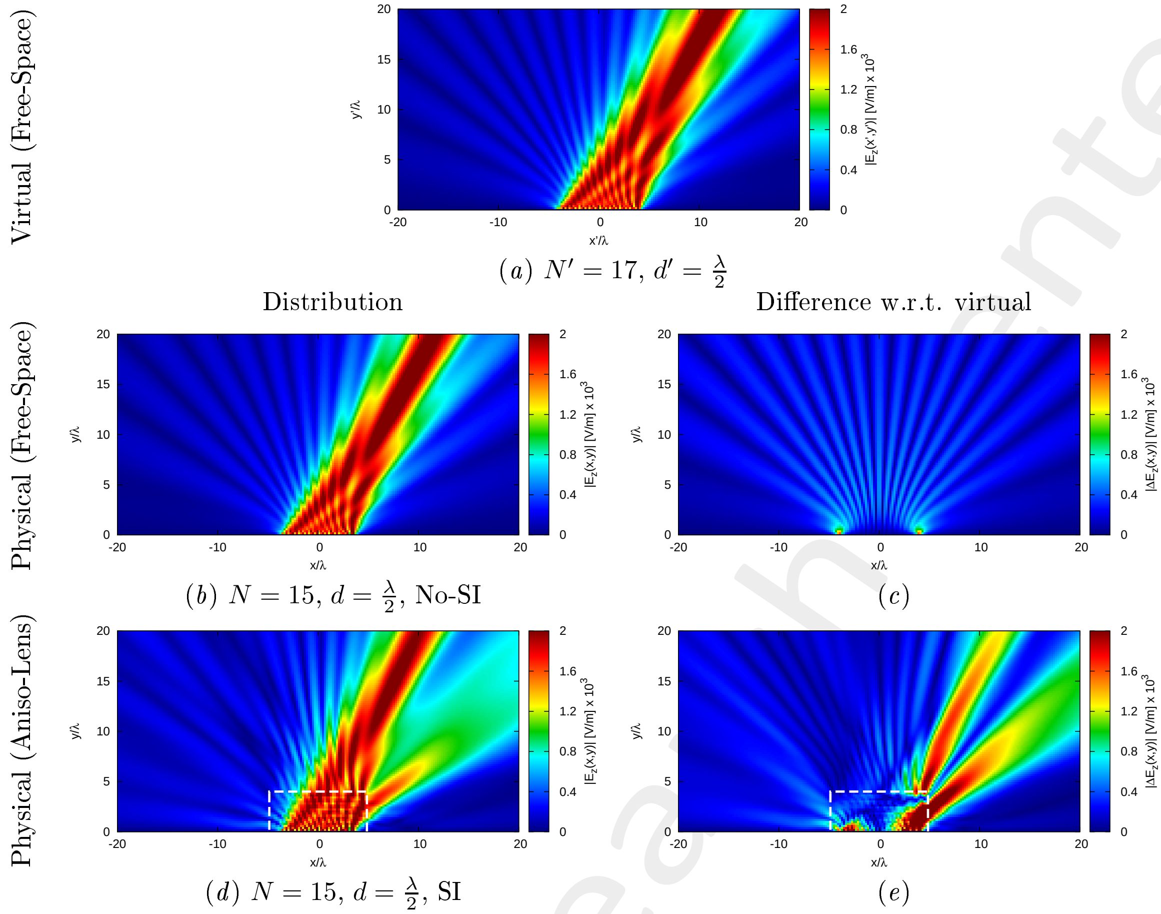

Figure 14: $\phi_s = 90$ [deg], $f = 600$ [MHz] - Electric field distributions.

Case $w' = 12.1$ **[λ],** $N' = 18$

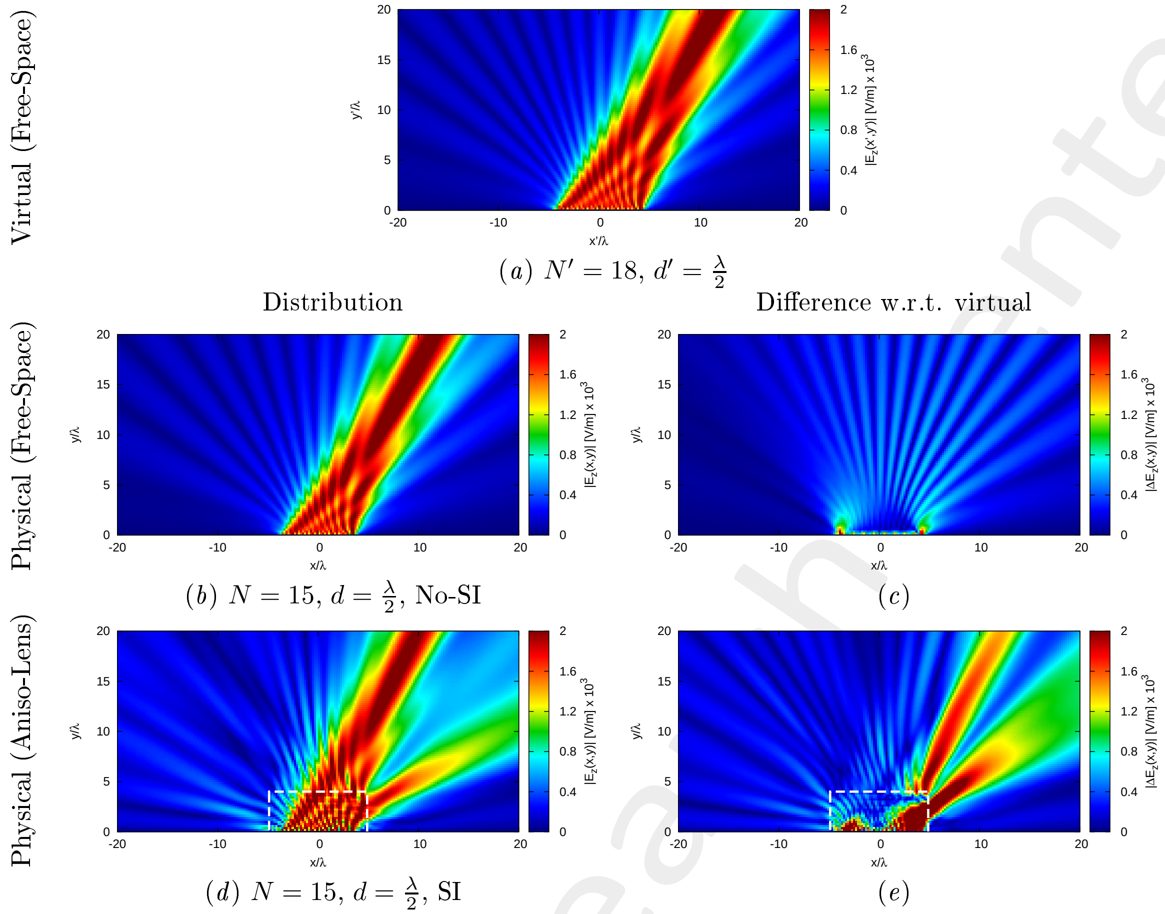

Figure 15: $\phi_s = 90$ [deg], $f = 600$ [MHz] - Electric field distributions.

Case $w' = 12.9$ **[**λ**],** $N' = 19$

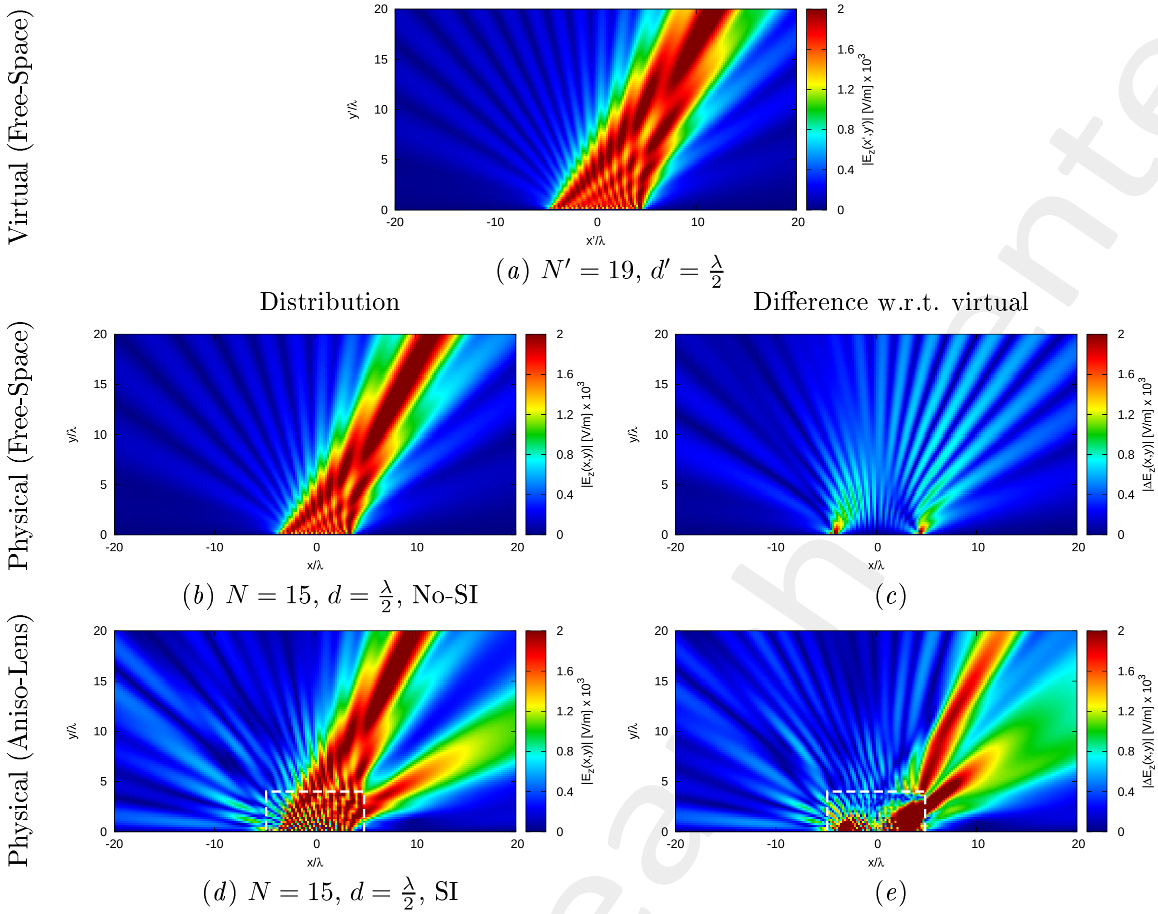

Figure 16: $\phi_s = 90$ [deg], $f = 600$ [MHz] - Electric field distributions.

Case $w' = 13.6$ **[**λ**]**, $N' = 20$

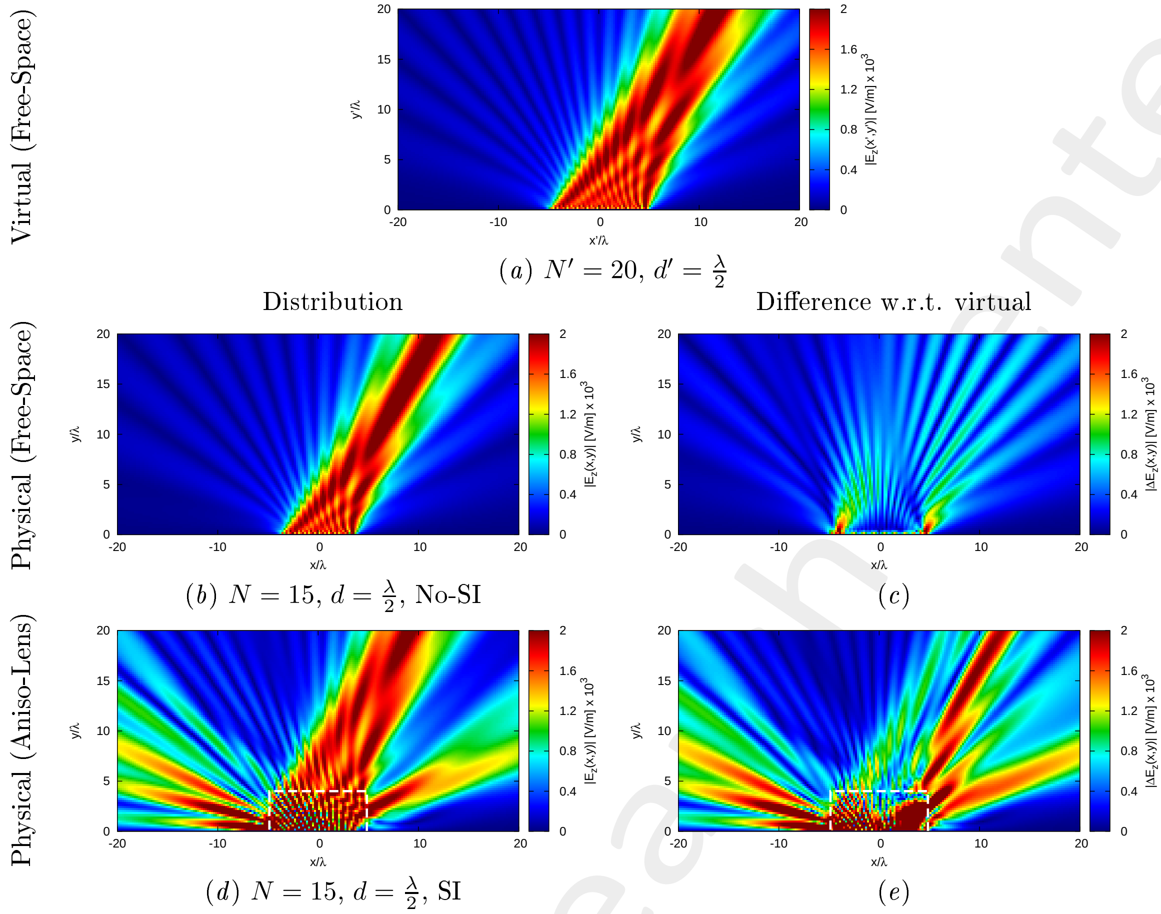

Figure 17: $\phi_s = 90$ [deg], $f = 600$ [MHz] - Electric field distributions.

1.3.4 Far-Field Patterns ($\phi_s = 90$ [deg], $f = 600$ [MHz])

Anisotropic Lens

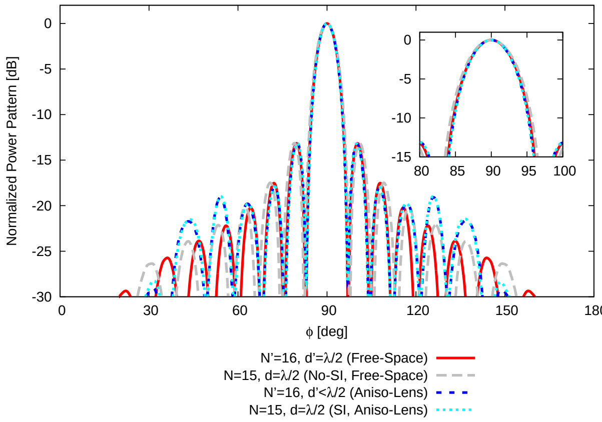

$(a)\ w' = 10.3\ [\lambda],\ N' = 16$

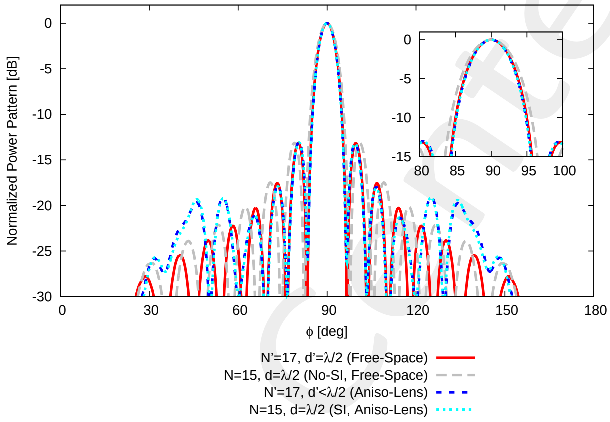

$(b)\ w' = 11.3\ [\lambda],\ N' = 17$

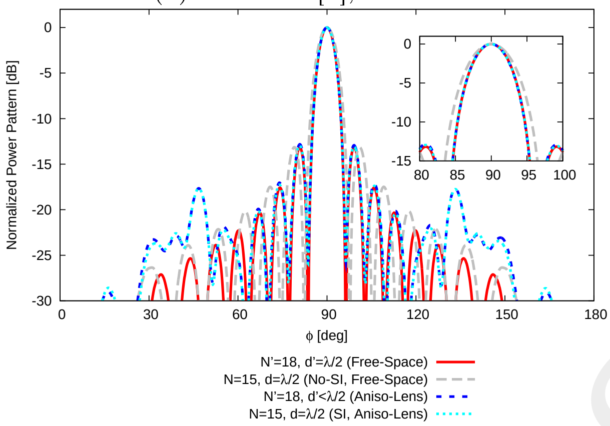

$(c)\ w' = 12.1\ [\lambda],\ N' = 18$

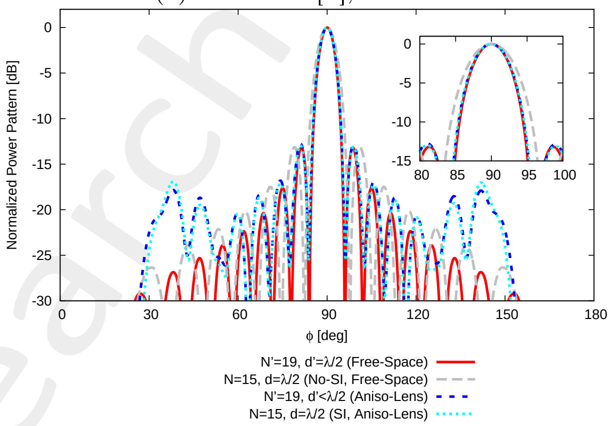

$(d)\ w' = 12.9\ [\lambda],\ N' = 19$

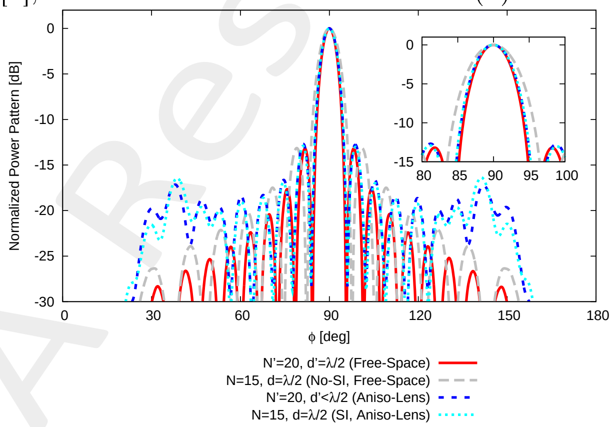

$(e)\ w' = 13.6\ [\lambda],\ N' = 20$

Figure 18: $\phi_s = 90$ [deg], $f = 600$ [MHz] - Far field pattern comparison for different values of w'.

1.3.5 Far-Field Patterns ($\phi_s = 75$ [deg], $f = 600$ [MHz])

Anisotropic Lens

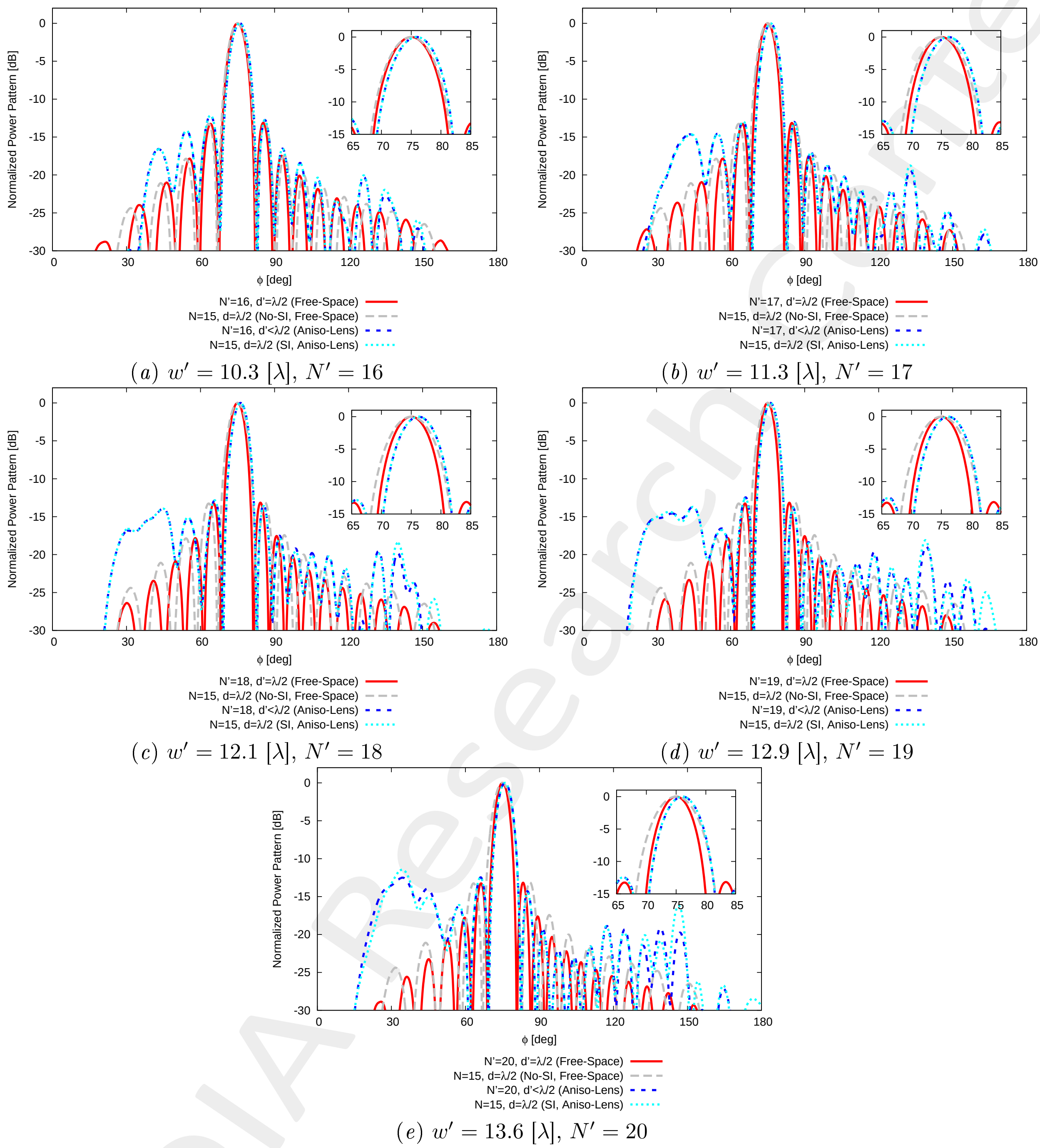

Figure 19: $\phi_s = 75$ [deg], $f = 600$ [MHz] - Far field pattern comparison for different values of w'.

1.3.6 Far-Field Patterns ($\phi_s = 60$ [deg], $f = 600$ [MHz])

Anisotropic Lens

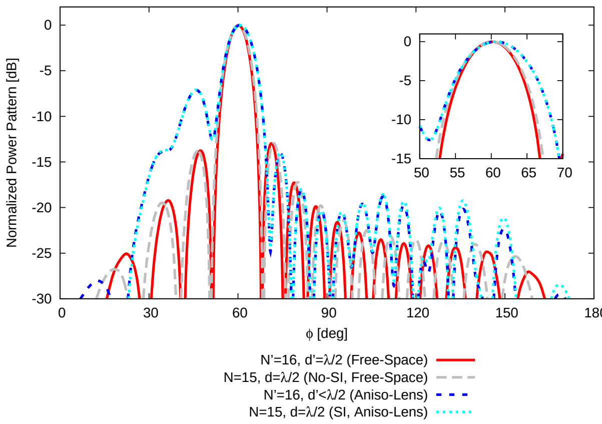

(a) $w' = 10.3$ [λ], $N' = 16$

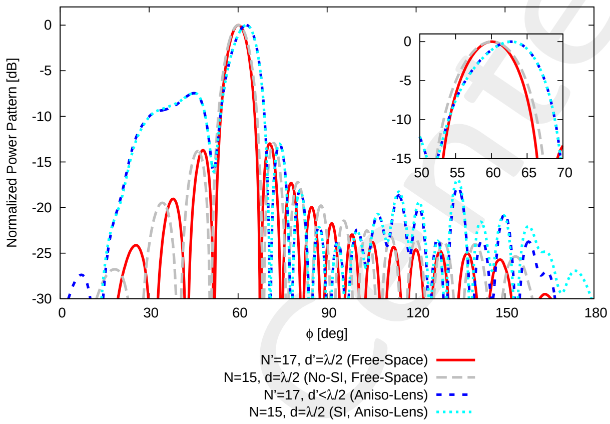

(b) $w' = 11.3$ [λ], $N' = 17$

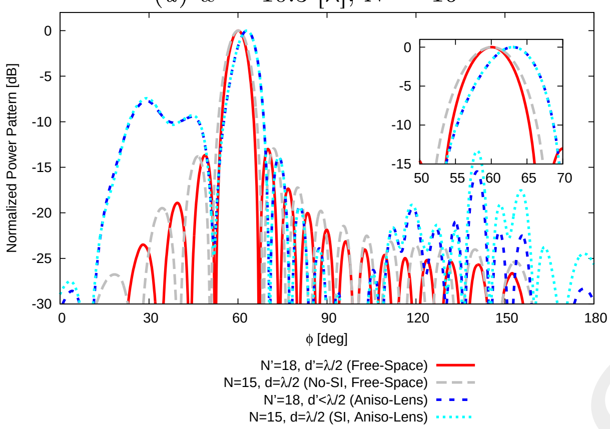

(c) $w' = 12.1$ [λ], $N' = 18$

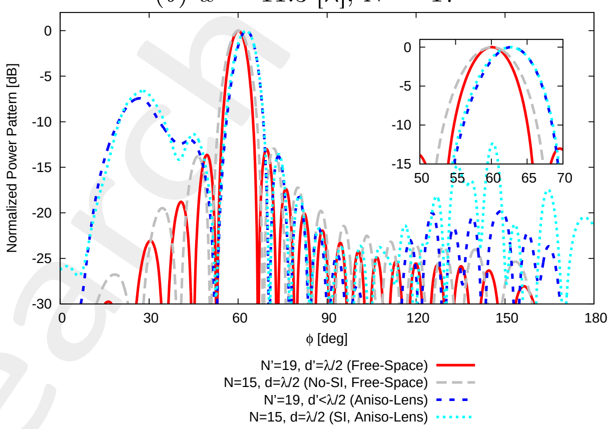

(d) $w' = 12.9$ [λ], $N' = 19$

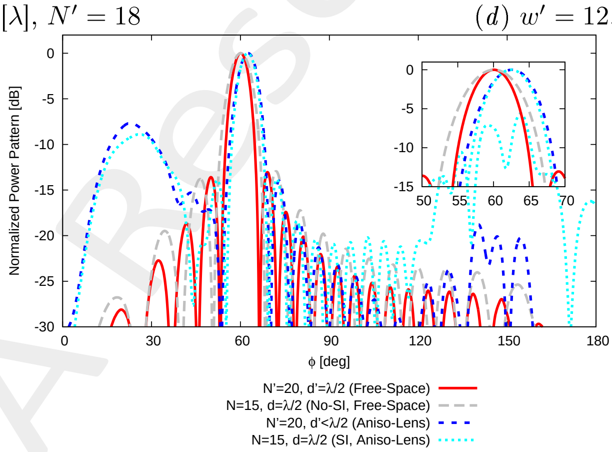

(e) $w' = 13.6$ [λ], $N' = 20$

Figure 20: $\phi_s = 60$ [deg], $f = 600$ [MHz] - Far field pattern comparison for different values of w'.

1.3.7 Final Summary: Performances vs. w' (vs. N')

Anisotropic Lens - $\phi_s = 90$ [deg]

This figure compares the pattern characteristics of

1. Original array ($N = 15$ elements, $d = \lambda/2$, Free-Space) - GREY;

2. Target array ($N' > N$ elements, $d = \lambda/2$, Free-Space) - RED;

3. QCTO-SI array ($N = 15$ elements, $d = \lambda/2$, Anisotropic Lens + SI) - CYAN;

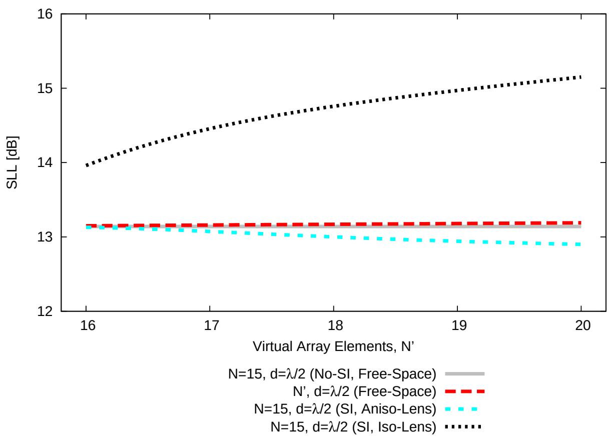

(a) SLL

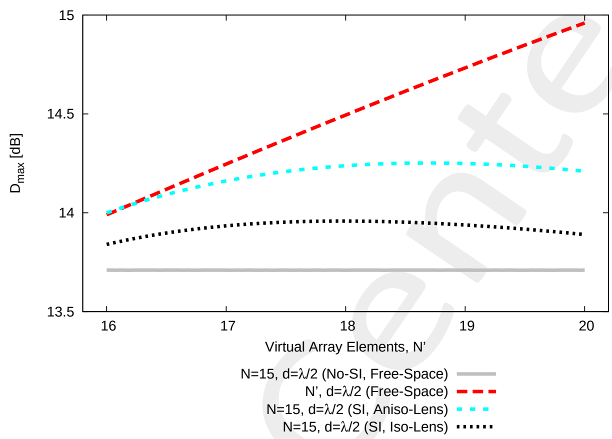

(b) $D_{\max}$

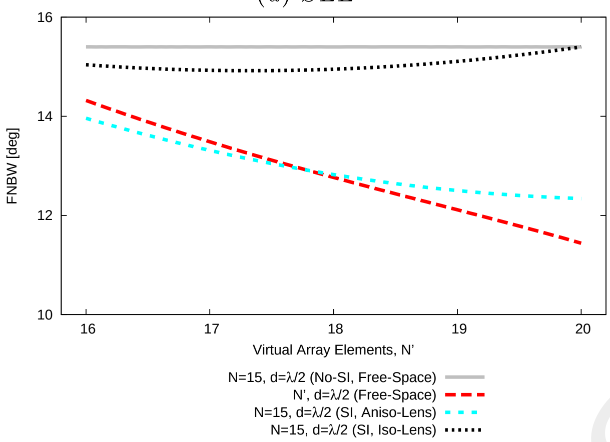

(b) $FNBW$

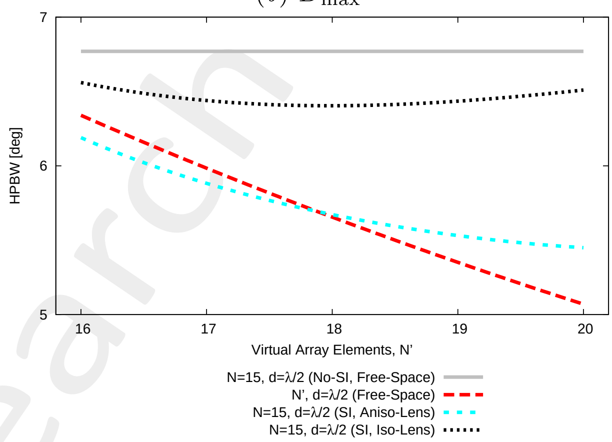

(c) $HPBW$

Figure 21: Aniso-Lens, $f = 600$ [MHz] - Pattern performances vs w' (vs. N').

Anisotropic Lens - $\phi_s = 75$ [deg]

This figure compares the pattern characteristics of

1. Original array ($N = 15$ elements, $d = \lambda/2$, Free-Space) - GREY;
2. Target array ($N' > N$ elements, $d = \lambda/2$, Free-Space) - RED;
3. QCTO-SI array ($N = 15$ elements, $d = \lambda/2$, Anisotropic Lens + SI) - CYAN;

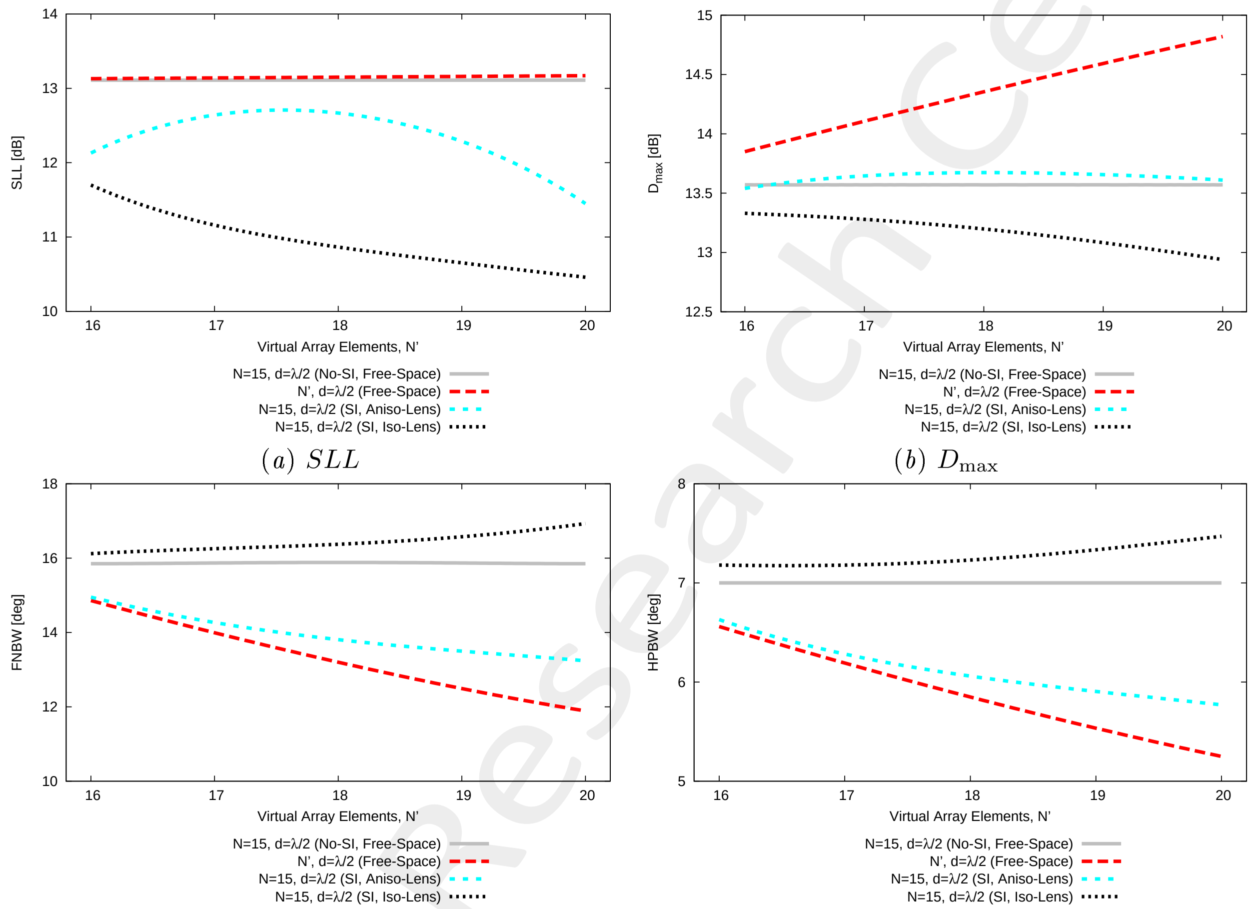

(a) SLL (b) $D_{\max}$

(b) $FNBW$ (c) $HPBW$

Figure 22: Aniso-Lens, $f = 600$ [MHz] - Pattern performances vs w' (vs. N').

Anisotropic Lens - $\phi_s = 60$ **[deg]**

This figure compares the pattern characteristics of

1. Original array ($N = 15$ elements, $d = \lambda/2$, Free-Space) - GREY;
2. Target array ($N' > N$ elements, $d = \lambda/2$, Free-Space) - RED;
3. QCTO-SI array ($N = 15$ elements, $d = \lambda/2$, Anisotropic Lens + SI) - CYAN;

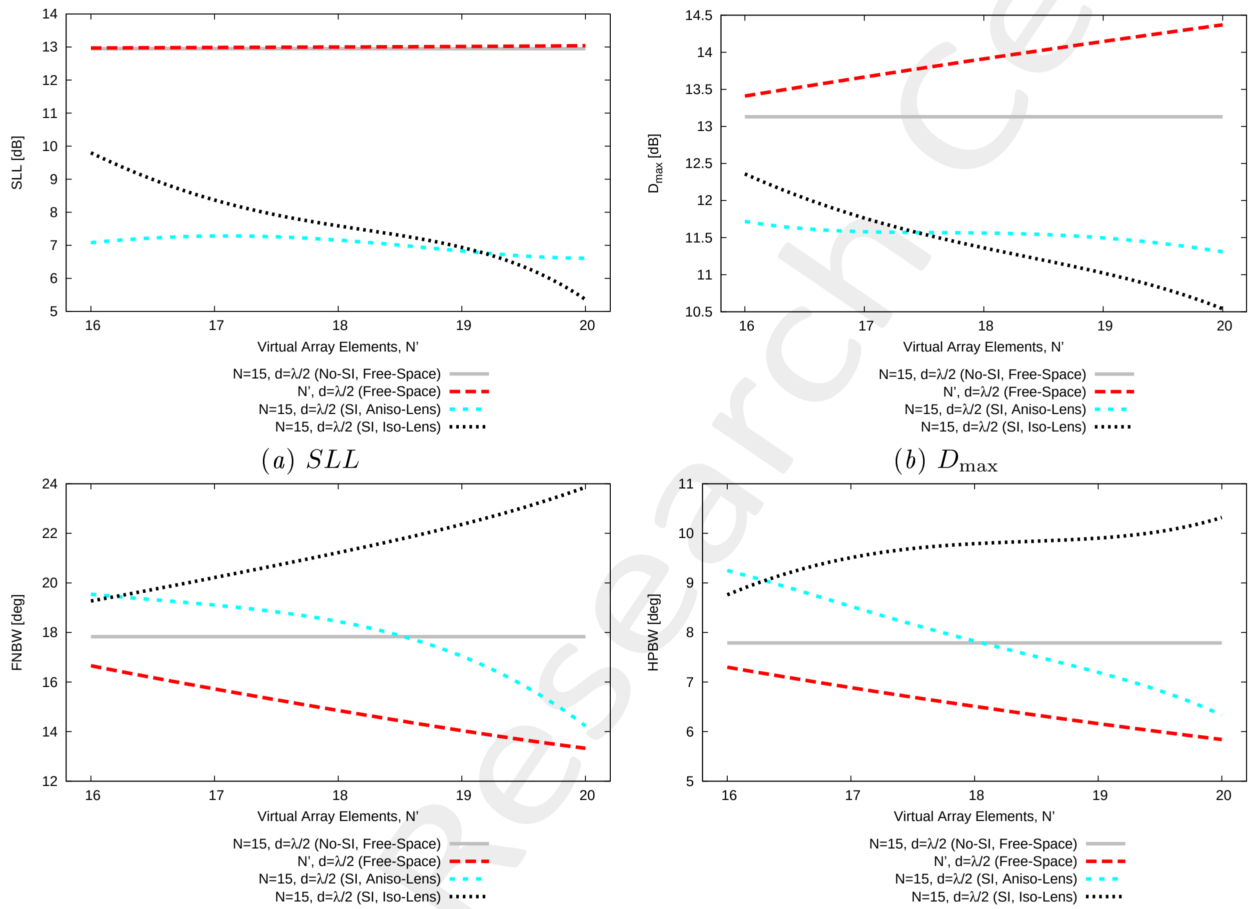

(a) SLL (b) $D_{\max}$

(b) $FNBW$ (c) $HPBW$

Figure 23: Aniso-Lens, $f = 600$ [MHz] - Pattern performances vs w' (vs. N').

1.3.8 Conclusions

- Good performances can be achieved when considering a broadside steering (i.e., $\phi_s = 90$ deg);
- Unfortunately, this is not true when considering a steering of the main beam.
- One of the main cause of such a degradation is due to the fact that the lens is not long enough along the x axis. Thus, when the array is steered, the beam propagates towards the corners of the lens, and this lead to both beam tilting and to an increase of the SLL.

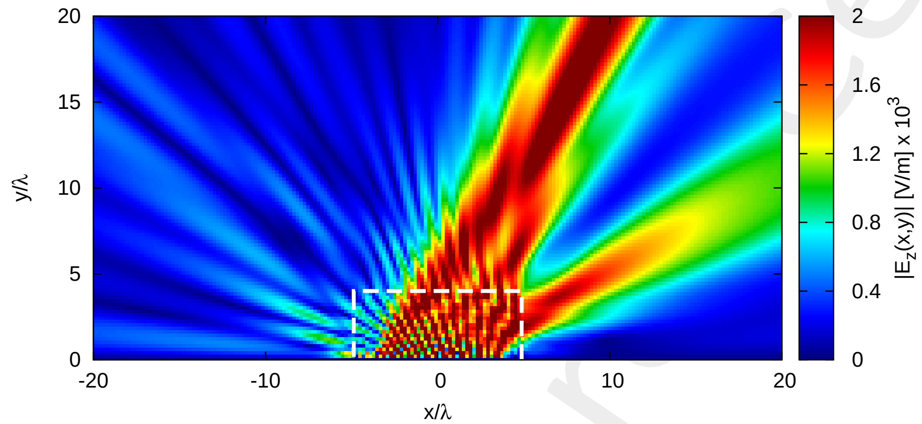

Figure 24: Case $w' = 12.9$ [λ], $N' = 19$ - Near field radiated by the physical-SI array ($N = 15$ elements, $d = \lambda/2$) when considering a steering of $\phi_s = 60$ deg. The beam partially propagates towards the upper right corner of the lens.

- In order to obtain better performances in steering, we need to enlarge the lens along the x-direction, such that to avoid that the steered beams propagates towards the corners of the lens.

References

[1] G. Oliveri, G. Gottardi, F. Robol, A. Polo, L. Poli, M. Salucci, M. Chuan, C. Massagrande, P. Vinetti, M. Mattivi, R. Lombardi, and A. Massa, "Co-design of unconventional array architectures and antenna elements for 5G base station," *IEEE Trans. Antennas Propag.*, vol. 65, no. 12, pp. 6752-6767, Dec. 2017.

[2] P. Rocca, G. Oliveri, R. J. Mailloux, and A. Massa, "Unconventional phased array architectures and design methodologies - A review," *Proc. IEEE*, vol. 104, no. 3, pp. 544-560, Mar. 2016.

[3] G. Oliveri, M. Salucci, N. Anselmi and A. Massa, "Multiscale System-by-Design synthesis of printed WAIMs for waveguide array enhancement," *IEEE J. Multiscale Multiphysics Computat. Techn.*, vol. 2, pp. 84-96, 2017.

[4] A. Massa and G. Oliveri, "Metamaterial-by-Design: Theory, methods, and applications to communications and sensing - Editorial," *EPJ Applied Metamaterials*, vol. 3, no. E1, pp. 1-3, 2016.

[5] L. Poli, G. Oliveri, P. Rocca, M. Salucci, and A. Massa, "Long-Distance WPT Unconventional Arrays Synthesis," *J. Electromagnet. Wave.*, vol. 31, no. 14, pp. 1399-1420, Jul. 2017.

[6] G. Oliveri, F. Viani, N. Anselmi, and A. Massa, "Synthesis of multi-layer WAIM coatings for planar phased arrays within the system-by-design framework," *IEEE Trans. Antennas Propag.*, vol. 63, no. 6, pp. 2482-2496, Jun. 2015.

[7] G. Oliveri, L. Tenuti, E. Bekele, M. Carlin, and A. Massa, "An SbD-QCTO approach to the synthesis of isotropic metamaterial lenses," *IEEE Antennas Wireless Propag. Lett.*, vol. 13, pp. 1783-1786, 2014.

[8] G. Oliveri, D. H. Werner, and A. Massa, "Reconfigurable electromagnetics through metamaterials - A review" *Proc. IEEE*, vol. 103, no. 7, pp. 1034-1056, Jul. 2015.

[9] G. Oliveri, E. T. Bekele, M. Salucci, and A. Massa, "Transformation electromagnetics miniaturization of sectoral and conical horn antennas," *IEEE Trans. Antennas Propag.*, vol. 64, no. 4, pp. 1508-1513, Apr. 2016.

[10] G. Oliveri, E. T. Bekele, M. Salucci, and A. Massa, "Array miniaturization through QCTO-SI metamaterial radomes," *IEEE Trans. Antennas Propag.*, vol. 63, no. 8, pp. 3465-3476, Aug. 2015.

[11] G. Oliveri, E. T. Bekele, D. H. Werner, J. P. Turpin, and A. Massa, "Generalized QCTO for metamaterial-lens-coated conformal arrays," *IEEE Trans. Antennas Propag.*, vol. 62, no. 8, pp 4089-4095, Aug. 2014.

[12] G. Oliveri, E. Bekele, M. Carlin, L. Tenuti, J. Turpin, D. H. Werner, and A. Massa, "Extended QCTO for innovative antenna system designs," IEEE Antenna Conference on Antenna Measurements and Applications (CAMA 2014), pp. 1-3, Nov. 16-19, 2014.

[13] G. Oliveri, P. Rocca, M. Salucci, E. T. Bekele, D. H. Werner, and A. Massa, "Design and synthesis of innovative metamaterial-enhanced arrays," IEEE International Symposium on Antennas Propag. (APS/URSI 2013), Orlando, Florida, USA, pp. 972 - 973, Jul. 7-12, 2013.

[14] G. Oliveri, "Improving the reliability of frequency domain simulators in the presence of homogeneous metamaterials - A preliminary numerical assessment," *Progress In Electromagnetics Research*, vol. 122, pp. 497-518, 2012.

[15] M. Salucci, G. Oliveri, N. Anselmi, G. Gottardi, and A. Massa, "Performance enhancement of linear active electronically-scanned arrays by means of MbD-synthesized metalenses," *J. Electromagnet. Wave.*, vol. 0, no. 0, pp. 1-29, 2017 (DOI: 10.1080/09205071.2017.1410077).